AGU100 ADVANCING EARTH AND SPACE SCIENCE

JGR

Journal of Geophysical Research: Space Physics

RESEARCH ARTICLE
10.1029/2018JA025666

Key Points:
- An electromagnetic particle-in-cell code is developed for dipole geometry
- This code is used to investigate self-consistent evolution of fast magnetosonic waves in the radial direction
- The warm plasma effect on wave propagation is examined

Correspondence to:
K. Min,
kyungguk@me.com

Citation:
Min, K., Liu, K., Denton, R. E., & Boardsen, S. A. (2018). Particle-in-cell simulations of the fast magnetosonic mode in a dipole magnetic field: 1-D along the radial direction. *Journal of Geophysical Research: Space Physics*, *123*, 7424–7440. https://doi.org/10.1029/2018JA025666

Received 10 MAY 2018
Accepted 28 AUG 2018
Accepted article online 30 AUG 2018
Published online 12 SEP 2018

©2018. American Geophysical Union. All Rights Reserved.

Particle-in-Cell Simulations of the Fast Magnetosonic Mode in a Dipole Magnetic Field: 1-D Along the Radial Direction

Kyungguk Min[1,2], Kaijun Liu[3], Richard E. Denton[4], and Scott A. Boardsen[5,6]

[1]Space Science Institute, Boulder, CO, USA, [2]Korea Astronomy and Space Science Institute, Daejeon, South Korea, [3]Department of Physics, Auburn University, Auburn, AL, USA, [4]Department of Physics and Astronomy, Dartmouth College, Hanover, NH, USA, [5]Goddard Planetary Heliophysics Institute, University of Maryland, Baltimore County, MD, USA, [6]NASA/GSFC, Greenbelt, MD, USA

Abstract An electromagnetic particle-in-cell code is used to investigate self-consistent evolution of the fast magnetosonic mode in a one-dimensional configuration along the radial direction in a dipole background magnetic field. A previous observation of this wave mode is used to select the simulation parameters. A partial shell velocity distribution of energetic protons with a moderate pitch angle anisotropy is used to excite the waves self-consistently. Consistent with local linear theory analysis, wave growth occurs only at exact harmonics of the local proton cyclotron frequency, Ω_p. However, radial propagation quickly removes the waves from the region where they can grow, leading to a time scale of wave amplification much longer than that predicted by linear theory. In addition, radial propagation from multiple wave sources makes the frequency spectrum measured at a single point much broader. The warm background plasma plays an important role in two ways. First, it increases the phase speed of the fast magnetosonic mode; and second, it causes the breakup of the extraordinary mode dispersion relation in the vicinity of the harmonics, where the broken dispersion curves are connected with multiple ion Bernstein modes. In this case, the waves propagating radially are absorbed at locations where their frequency reaches integer multiples of Ω_p and background protons experience perpendicular heating at those locations.

1. Introduction

Fast magnetosonic waves, also known as equatorial noise (Russell et al., 1970), are among the most frequently observed plasma waves in the inner magnetosphere (Boardsen et al., 2016; Hrbáčková et al., 2015; Ma et al., 2013; Meredith et al., 2008; Němec et al., 2005; Posch et al., 2015; Santolík et al., 2004; Tsurutani et al., 2014). Observations show that fast magnetosonic waves are primarily confined to a narrow latitudinal range about the magnetic equator and occur both inside and outside of the plasmapause at a wide range of radial distances (Boardsen et al., 2016; Hrbáčková et al., 2015; Němec et al., 2005, 2013; Posch et al., 2015; Santolík et al., 2004). The polarization of the magnetic and electric field fluctuations, $|\delta B_\parallel| \gg |\delta B_\perp|$ and $|\delta E_\perp| \gg |\delta E_\parallel|$, indicate wave propagation very oblique/quasi-perpendicular to the background magnetic field, $\mathbf{B}_0$ (Boardsen et al., 1992; Kasahara et al., 1994; Laakso et al., 1990; Perraut et al., 1982; Santolík et al., 2002), where δB and δE denote the fluctuating magnetic and electric fields, respectively, and $\perp$ and $\parallel$ denote directions perpendicular and parallel to $\mathbf{B}_0$, respectively. The frequency spectrum typically shows a series of spectral peaks, often spaced at multiples of the proton cyclotron frequency (f_{cp}), spanning from about f_{cp} to about the lower hybrid resonant frequency (Balikhin et al., 2015; Boardsen et al., 2016; Min et al., 2018). Linear theory and kinetic simulations suggest that proton ring/shell velocity distributions with ring/shell speed $v_r \gtrsim v_A$ can drive growing modes at f_{cp} and its harmonics, where v_A is the Alfvén speed (Boardsen et al., 1992; Chen et al., 2010; Gulelmi et al., 1975; Horne et al., 2000; K. Liu et al., 2011; Perraut et al., 1982). Observations indeed show that the fast magnetosonic waves are often associated with proton ring distributions in the inner magnetosphere (Balikhin et al., 2015; Ma, Li, Chen, Thorne, & Angelopoulos, 2014; Min et al., 2018).

The fact that the electric field fluctuations are strongly longitudinal (i.e., $\mathbf{k} \cdot \boldsymbol{\delta E} \approx k\delta E$) and the wave normal directions are quasi-perpendicular to $\mathbf{B}_0$ allows observational determination of the propagation direction (Santolík et al., 2002). Němec et al. (2013) analyzed 10 years of Cluster observations and showed statistically that azimuthal propagation is dominant where the (total) plasma density is low ($n_0 \lesssim 30\ \mathrm{cm}^{-3}$), as

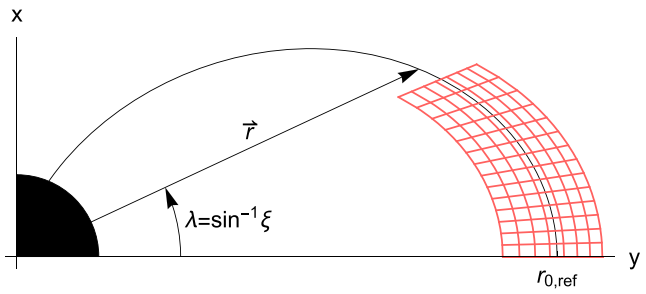

Figure 1. The dipole magnetic field line (black) and curvilinear grid mapping (red) presented on a meridional plane.

occurs outside the plasmapause, but no preferential propagation direction is found where the density is high ($n_0 \gtrsim 100$ cm^{-3}), as occurs inside the plasmapause. While the azimuthal direction may be the preferential direction of propagation outside the plasmapause where free energy source is typically located (e.g., Chen et al., 2010), the presence of the radial component in the propagation direction is believed to explain many observational features including, but not limited to, the occurrence of fast magnetosonic waves deep in the plasmasphere and off-harmonic frequency spectrum of the electric and magnetic field fluctuations (Horne et al., 2000; Perraut et al., 1982; Posch et al., 2015; Santolík et al., 2002, 2016; Zhima et al., 2015). Santolík et al. (2002) analyzed the fluctuating electric field to observationally confirm a radial component of the wave normal vector. Ray tracing studies suggest that the plasma and magnetic field gradients (dominantly in the radial direction) play an important role in trapping the fast magnetosonic mode (Chen & Thorne, 2012; Ma, Li, Chen, Thorne, Kletzing, et al., 2014). Recently, X. Liu et al. (2018) carried out a full wave simulation in the radial direction to explain the observational wave power truncated by fine-scale density structures.

The present study uses an electromagnetic particle-in-cell (PIC) code in a dipole magnetic field to provide a first-principles description of the evolution of the fast magnetosonic mode. We first generalize the PIC code of K. Liu (2007) to dipole geometry and then use this code to investigate the excitation and propagation of the fast magnetosonic mode in a one-dimensional configuration. Similar to X. Liu et al. (2018), we only allow radial variation. Unlike X. Liu et al. (2018), however, we assume a uniform background plasma for simplicity, hence excluding the effects of a density gradient and the small-scale density variations that they examined. But our code describes the fully kinetic self-consistent evolution of the waves.

Section 2 describes the PIC model, and section 3 presents the initial setup and local linear instability analysis. Section 4 presents the simulation results and section 5 provides a summary and discussions.

2. Model Description

The electromagnetic PIC code developed by K. Liu (2007) is modified to use dipole geometry. The subsections here describe some of the essential components for this generalization.

2.1. Curvilinear Coordinates

The present study employs nonorthogonal curvilinear coordinates to naturally accommodate curved magnetic field geometry. In accordance with the diagram in Figure 1, we define spherical coordinates (ξ, r, ϕ)

$$\begin{pmatrix} x \\ y \\ z \end{pmatrix} = \begin{pmatrix} r\xi \\ r\sqrt{1-\xi^2}\cos\phi \\ r\sqrt{1-\xi^2}\sin\phi \end{pmatrix}, \tag{1}$$

where $-1 \le \xi \le 1$ is the sine of the latitude ($\xi = \sin\lambda$) and $-\pi \le \phi < \pi$ is the azimuthal angle. The corresponding unit vectors are given by

$$\begin{aligned} \mathbf{e}_\xi &= \sqrt{1-\xi^2}\mathbf{e}_x - \xi\cos\phi\mathbf{e}_y - \xi\sin\phi\mathbf{e}_z \\ \mathbf{e}_r &= \xi\mathbf{e}_x + \sqrt{1-\xi^2}\cos\phi\mathbf{e}_y + \sqrt{1-\xi^2}\sin\phi\mathbf{e}_z \\ \mathbf{e}_\phi &= -\sin\phi\mathbf{e}_y + \cos\phi\mathbf{e}_z, \end{aligned} \tag{2}$$

and the scale factors are $h_\xi = r/\sqrt{1-\xi^2}$, $h_r = 1$, and $h_\phi = r\sqrt{1-\xi^2}$. The dipole magnetic field is $\mathbf{B} = B_0(\sqrt{1-\xi^2}\mathbf{e}_\xi - 2\xi\mathbf{e}_r)/(1-\xi^2)^3$ and the field line equation is $r = r_0(1-\xi^2)$ (Roederer, 1970), where B_0 is the magnetic field magnitude at the equator ($\xi = 0$) of a field line and r_0 is the equatorial distance to the field line (field line label). Note that B_0 is a function of r_0 ($B_0 \propto r_0^{-3}$).

We choose the following curvilinear coordinates (q^1, q^2, q^3):

$$\begin{pmatrix} q^1 \\ q^2 \\ q^3 \end{pmatrix} = \begin{pmatrix} \frac{r_{0,\mathrm{ref}}}{\Delta_1} \int (1-\xi^2)^3 \mathrm{d}\xi \\ \frac{r_{0,\mathrm{ref}}}{3\Delta_2} \frac{r_0^3}{r_{0,\mathrm{ref}}^3} \\ \frac{r_{0,\mathrm{ref}}}{\Delta_3} \phi \end{pmatrix}, \tag{3}$$

where $r_{0,\mathrm{ref}}$ is the equatorial distance to a reference field line (used to determine the relative scales), and Δ_j with $j = 1, 2, 3$ are the constant scale lengths of the corresponding coordinates. The q^3 coordinate is essentially ϕ with a constant scale factor and is orthogonal to the other two coordinates. The q^1 coordinate varies along the dipole magnetic field line and is obtained by integrating

$$\frac{\Delta_1}{r_{0,\mathrm{ref}}} \mathrm{d}q^1 = \frac{\mathrm{d}s/r_0}{B/B_0}, \tag{4}$$

where $\mathrm{d}s = r_0\sqrt{1+3\xi^2}\mathrm{d}\xi$ is the field line arc length (Roederer, 1970) and $B \equiv |\mathbf{B}| = B_0\sqrt{1+3\xi^2}/(1-\xi^2)^3$. Equation (4) states that the field line arc length corresponding to a unit length in the q^1 coordinate is proportional to B for a given field line r_0. Finally, the q^2 coordinate varies along r_0 and is obtained by integrating $\Delta_2 \mathrm{d}q^2 = (r_0/r_{0,\mathrm{ref}})^2 \mathrm{d}r_0$. The r_0^2 dependence ensures that the differential volume element $\mathrm{d}V$ is constant (independent of position; more discussion in the next paragraph). The introduction of Δ_j is to factor out the scale lengths from the curvilinear coordinates, q^j, which are then dimensionless. In particular, the physical size corresponding to $\Delta q^j = 1$ at $\xi = 0$ and $r_0 = r_{0,\mathrm{ref}}$ is approximately Δ_j. When discretizing the grid space in the simulations, we choose Δ_j to make the grid size unity (i.e., $\Delta q^1 \times \Delta q^2 \times \Delta q^3 = 1 \times 1 \times 1$). Therefore in the simulations, the difference $q^j_{\mathrm{max}} - q^j_{\mathrm{min}}$ represents the number of grid points in the jth coordinate direction, where q^j_{max} and q^j_{min} are the curvilinear locations of the maximum and minimum boundaries, respectively. Figure 1 displays the mapping of curvilinear grid space in a meridional plane.

The nonorthogonal curvilinear coordinates require a general vector analysis using a covariant and contravariant formalism (Danielson, 1992). The covariant basis vectors and the contravariant basis vectors are given by $\mathbf{g}_j = \partial\mathbf{r}/\partial q^j$ and $\mathbf{g}^j = \nabla q^j$, respectively. These two sets of basis vectors are related to each other through $\mathbf{g}_i = \sqrt{g}\mathbf{g}^j \times \mathbf{g}^k$ and $\mathbf{g}^i = \mathbf{g}_j \times \mathbf{g}_k/\sqrt{g}$, where i, j, and k are chosen cyclically from 1, 2, and 3, and $\sqrt{g} = \mathbf{g}_1 \cdot (\mathbf{g}_2 \times \mathbf{g}_3) = (\mathbf{g}^1 \cdot (\mathbf{g}^2 \times \mathbf{g}^3))^{-1}$. (Here g is the determinant of metric coefficients, $g_{ij} = \mathbf{g}_i \cdot \mathbf{g}_j$, Danielson, 1992.) The contravariant and covariant basis vectors for the curvilinear coordinates of equation (3) may, respectively, read

$$\begin{aligned} \mathbf{g}^1 &= \frac{1}{\Delta_1} \frac{r_{0,\mathrm{ref}}}{r} (1-\xi^2)^{7/2} \mathbf{e}_\xi \\ \mathbf{g}^2 &= \frac{1}{\Delta_2} \frac{(r_0/r_{0,\mathrm{ref}})^3}{r/r_{0,\mathrm{ref}}} \left[\frac{2\xi}{\sqrt{1-\xi^2}} \mathbf{e}_\xi + \mathbf{e}_r \right] \\ \mathbf{g}^3 &= \frac{1}{\Delta_3} \frac{r_{0,\mathrm{ref}}/r}{\sqrt{1-\xi^2}} \mathbf{e}_\phi \end{aligned} \tag{5}$$

and

$$\begin{aligned} \mathbf{g}_1 &= \frac{\Delta_1}{\sqrt{1-\xi^2}} \frac{(r_0/r_{0,\mathrm{ref}})^3}{r^2/r_{0,\mathrm{ref}}^2} \left[\mathbf{e}_\xi - \frac{2\xi}{\sqrt{1-\xi^2}} \mathbf{e}_r \right] \\ \mathbf{g}_2 &= \frac{\Delta_2}{\sqrt{1-\xi^2}} \frac{r_{0,\mathrm{ref}}^2}{r^2} (1-\xi^2)^{7/2} \mathbf{e}_r \\ \mathbf{g}_3 &= \Delta_3 \frac{r}{r_{0,\mathrm{ref}}} \sqrt{1-\xi^2} \mathbf{e}_\phi. \end{aligned} \tag{6}$$

By definition, $\mathbf{g}_1 \| \mathbf{B}$ and $\mathbf{g}^2 \perp \mathbf{B}$. Also, it is straightforward to show that $\sqrt{g} = \Delta_1\Delta_2\Delta_3$. A salient feature of the present curvilinear coordinates is that the differential volume element is independent of position, $\mathrm{d}V \equiv \sqrt{g}\mathrm{d}q^1\mathrm{d}q^2\mathrm{d}q^3$. This is useful not only for differential geometry but also for loading and weighing simulation particles (e.g., $\nabla \cdot \mathbf{u} = \frac{1}{\sqrt{g}} \frac{\partial(\sqrt{g}u^j)}{\partial q^j} = \partial u^j/\partial q^j$ and $\int \mathrm{d}V = \sqrt{g} \int\int\int \mathrm{d}q^1\mathrm{d}q^2\mathrm{d}q^3$).

A vector $\mathbf{u}$ can be expressed in terms of the covariant basis vectors, $\mathbf{u} = u^j\mathbf{g}_j$, or of the contravariant basis vectors, $\mathbf{u} = u_j\mathbf{g}^j$, where the summation over the repeated indices is assumed. One can use the identity $\mathbf{g}_i \cdot \mathbf{g}^j = \delta_i^j$ to get jth contravariant ($u^j = \mathbf{u} \cdot \mathbf{g}^j$) and covariant ($u_j = \mathbf{u} \cdot \mathbf{g}_j$) vector components, where $\delta_i^j = 1$ for $i = j$ and 0 otherwise (Danielson, 1992).

2.2. PIC Scheme

The PIC code developed by K. Liu (2007) has been used to simulate whistler and fast magnetosonic/ion Bernstein plasma instabilities in a homogeneous plasma with a uniform background magnetic field (e.g., Fu et al., 2014; Gary et al., 2011; K. Liu et al., 2006, 2011; Min et al., 2016, 2018). We limit the model description to those relevant to the curvilinear coordinates and refer readers to K. Liu (2007) for many details of the PIC scheme adopted here.

We denote the σth species plasma frequency as $\omega_\sigma \equiv \sqrt{4\pi n_\sigma q_\sigma^2/m_\sigma}$, the σth species cyclotron frequency as $\Omega_\sigma \equiv q_\sigma B/m_\sigma c$, and the σth species plasma beta as $\beta_\sigma \equiv 8\pi n_\sigma T_\sigma/B^2$, where c is the light speed, n_σ is the number density, q_σ is the charge state, and m_σ is the rest mass of that species (cgs unit system). For the present study, $\sigma = e$ for electrons and p for protons. Internally, the following variables are used: $\vec{\Xi} \equiv (q_0/m_0 c)\mathbf{E}$ for the electric field (frequency units), $\vec{\Omega} \equiv (q_0/m_0 c)\mathbf{B}$ for the magnetic field (frequency units), $\vec{\mathcal{J}} \equiv (4\pi q_0/m_0 c)\mathbf{J}$ for the current density (units of frequency squared), and $\Pi \equiv (4\pi q_0/m_0)\rho$ for the charge density (units of frequency squared), where q_0 and m_0 are some reference charge and mass, respectively (those of protons in the present study), and **B** in this subsection shall mean the total magnetic field including both the static and perturbed parts. With these variables, Maxwell's equations read

$$\begin{aligned} \frac{\partial \vec{\Xi}}{\partial t} &= c\nabla \times \vec{\Omega} - \vec{\mathcal{J}} \\ \frac{\partial \vec{\Omega}}{\partial t} &= -c\nabla \times \vec{\Xi} \\ c\nabla \cdot \vec{\Xi} &= \Pi \\ c\nabla \cdot \vec{\Omega} &= 0, \end{aligned} \tag{7}$$

and the (nonrelativistic) equation of motion of particles reads $\mathrm{d}\mathbf{v}/\mathrm{d}t = (\Omega_\sigma/|\vec{\Omega}|)(c\vec{\Xi} + \mathbf{v} \times \vec{\Omega})$.

The time evolution of electric and magnetic field fluctuations is described by solving the first two of equations (7), which in the component form read (e.g., Eastwood et al., 1995)

$$\begin{aligned} \frac{\partial \Xi^i}{\partial t} &= c\,\frac{\epsilon^{ijk}}{\sqrt{g}}\frac{\partial \Omega_k}{\partial q^j} - \mathcal{J}^i \\ \frac{\partial \Omega^i}{\partial t} &= -c\,\frac{\epsilon^{ijk}}{\sqrt{g}}\frac{\partial \Xi_k}{\partial q^j}, \end{aligned} \tag{8}$$

where ϵ^{ijk} is the Levi-Civita symbol. Equation (8) involves covariant vector components in the curl operation. Conversion from the contravariant to covariant components of a vector **u** is given by $u_i = g_{ij}u^j$, where $g_{ij} = \mathbf{g}_i \cdot \mathbf{g}_j$ are the covariant metric coefficients (Danielson, 1992). Noting that the velocity vector is $\mathbf{v} = \dot{x}\mathbf{e}_x + \dot{y}\mathbf{e}_y + \dot{z}\mathbf{e}_z = \dot{q}^j\mathbf{g}_j$, the curvilinear coordinates of a particle are advanced by integrating $\mathrm{d}q^j/\mathrm{d}t = \mathbf{v} \cdot \mathbf{g}^j$ (Swift, 2007). On the other hand, it is simpler both numerically and mathematically to update velocities in the Cartesian coordinate system (e.g., Bagdonat & Motschmann, 2002; Hu & Denton, 2009). Therefore, conversions from the contravariant to Cartesian components are needed for the electric and magnetic fields before updating particle velocities. Likewise, the Cartesian components of the current density are collected after updating particle velocities and then converted to the contravariant components before updating the electric field.

For the present 1-D simulations in the radial (q^2) direction at the magnetic equator ($\xi = 0$), we set $\partial/\partial q^1 = \partial/\partial q^3 = 0$ and only keep the q^2 coordinate; however, all three velocity components are kept.

2.3. Boundary Conditions

The boundary conditions are perhaps the single most important factor for successful simulations. Similar to earlier simulation studies (e.g., Hu & Denton, 2009; Ke et al., 2017), reflecting boundary conditions are used for particles and open boundary conditions are used for waves.

Particles should be reflected not only to conserve the total energy but also not to generate any spurious current at the boundary (Hu, 2010). We adopt the method described by Hu, (2010; in turn derived from Naitou et al., 1979), which is summarized as follows. In the 2-D configuration on a meridional plane that these authors considered, when a particle hits one of the q^1 boundaries (the boundary surfaces roughly perpendicular to the background magnetic field), the particle's q^1 coordinate is replaced with $2q^1_{\mathrm{min,max}} - q^1$ and the sign of the velocity component parallel to the background magnetic field is flipped ($v_\parallel \rightarrow -v_\parallel$). When a particle hits

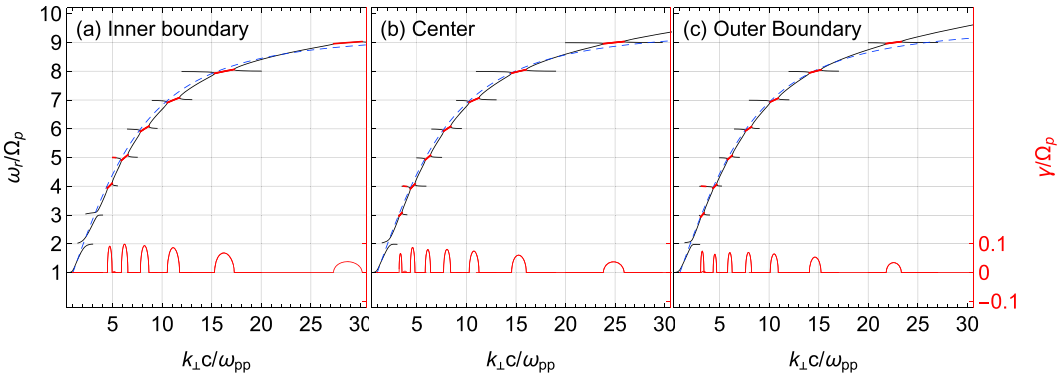

Figure 2. Local linear theory solutions for $k_{||} = 0$ (a) at the inner boundary, (b) at the center, and (c) at the outer boundary (for the case with cooler background protons). (These locations correspond to 3.52, 3.7, and 3.86 R_E, respectively.) The black and red curves show solutions for the real and imaginary parts of the complex frequency, and the blue dashed curves show the real frequency from the cold plasma extraordinary mode dispersion relation. Additionally, the regions where the imaginary part is positive are highlighted with red on the black curves. The frequency quantities are normalized to the local proton gyrofrequency, Ω_p, and the proton inertial length c/ω_{pp} is independent of position. The lower hybrid frequencies at the inner boundary, at the center, and at the outer boundary are $\omega_{lh}/\Omega_p = 9.33$, 9.49, and 9.60, respectively.

one of the q^2 boundaries (the boundary surfaces parallel to the background magnetic field), the particle's q^2 coordinate is replaced with $2q^2_{\mathrm{min,max}} - q^2$ and the sign of both velocity components perpendicular to the background magnetic field is flipped ($\mathbf{v}_\perp \rightarrow -\mathbf{v}_\perp$). Using the unit vector parallel to the background magnetic field $\mathbf{e}_1 \equiv \mathbf{g}_1/|\mathbf{g}_1|$, the velocity reflections can be achieved by $\mathbf{v} \rightarrow \mathbf{v} - 2(\mathbf{v}\cdot\mathbf{e}_1)\mathbf{e}_1$ for the q^1 reflection and $\mathbf{v} \rightarrow 2(\mathbf{v}\cdot\mathbf{e}_1)\mathbf{e}_1 - \mathbf{v}$ for the q^2 reflection. Note that the present 1-D simulations in the radial direction only require the q^2 reflection.

The outgoing electric and magnetic field fluctuations are absorbed using the masking method described by Umeda et al. (2001). For illustration, let us consider a 1-D domain in the x direction with length $L_x + 2L_D$, where L_x is the length of the interior region and L_D is the length of the masking region at each end (see Umeda et al., 2001; Figure 3). The coordinate varies between $-L_x/2 - L_D$ and $L_x/2 + L_D$. A masking function

$$f_M(x,r) = \begin{cases} 1 & \text{for } |x| \le L_x/2 \\ 1 - \left(r\frac{|x|-L_x/2}{L_D}\right)^2 & \text{for } |x| > L_x/2 \end{cases} \tag{9}$$

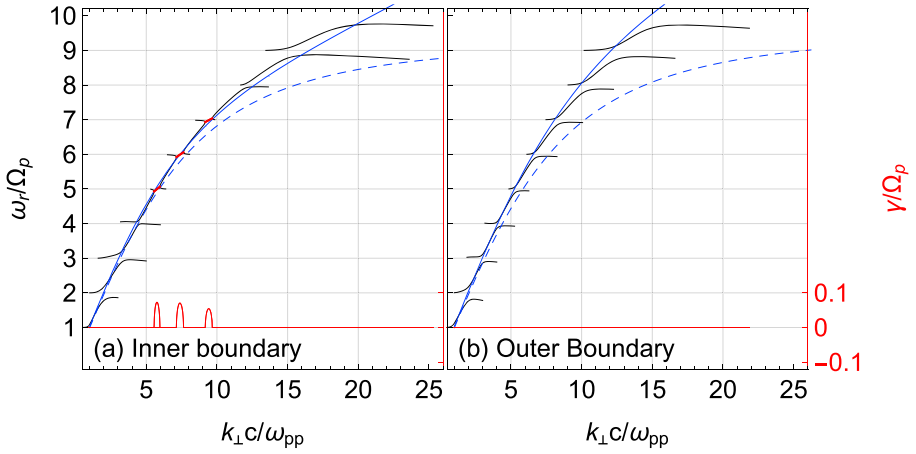

Figure 3. Local linear theory solutions at the (a) inner and (b) outer boundaries for the case with warmer background protons. The figure format is the same as in Figure 2. Additionally, the blue solid curves represent the MHD dispersion relation with thermal correction.

is applied at every update cycle to both the electric field and magnetic field as follows:

$$\vec{\Omega}^{t+\Delta t/2}(x) = f_M(x, r_d)\left[\vec{\Omega}^{t-\Delta t/2}(x) - \Delta t\left(c\nabla \times \vec{\Xi}^{t}(x)\right) f_M(x, r_r)\right]$$
$$\vec{\Xi}^{t+\Delta t}(x) = f_M(x, r_d)\left[\vec{\Xi}^{t}(x) + \Delta t\left(c\nabla \times \vec{\Omega}^{t+\Delta t/2}(x) - 4\pi\vec{J}^{t+\Delta t/2}(x)\right) f_M(x, r_r)\right], \quad (10)$$

where $0 \le r_d \le 1$ and $0 \le r_r \le 1$ are the amplitude damping and phase retardation factors, respectively. It is desirable to use L_D as small as possible to maximize the use of the simulation domain (by reducing the masking region). Umeda et al. (2001) suggests that in general, $r_d \sim 0.1$ and $r_r \sim 1$ result in the most effective damping of the outgoing waves.

2.4. Particle Loading

The simulation particles should be loaded to have a kinetic equilibrium along the field line. If a velocity distribution is isotropic at the magnetic equator, the density and temperature (or pressure) shall be invariant along the field line to satisfy equilibrium. If, on the other hand, the velocity distribution is anisotropic at the equator, the density and the pressure should vary along the field line accordingly. For a bi-Maxwellian distribution at the equator, the field line dependence of macroscopic quantities has been derived by Chan et al. (1994). In addition, for an equatorial velocity distribution of the form $f_0 \propto g(v_0)\sin^l\alpha_0$, Xiao and Feng (2006) showed that the distribution along the field line has the form $f \propto (B_0/B)^{l/2} g(v)\sin^l\alpha$, where $g(v)$ is a function of velocity magnitude, α is the pitch angle, l is the pitch angle anisotropy index, B is the magnitude of the local magnetic field, and the subscript 0 denotes equatorial values. Therefore, the pitch angle anisotropy $\frac{\int_0^\pi \sin^{3+l}\alpha d\alpha}{2\int_0^\pi \sin^{1+l}\alpha\cos^2\alpha d\alpha} = (2+l)/2$ is invariant and the density varies as $(B_0/B)^{l/2}$. This means that for an anisotropic distribution with an excess of perpendicular temperature (i.e., $l > 0$), the density is maximized at the equator, as also occurs for a bi-Maxwellian.

The present study uses a partial shell velocity distribution (Min et al., 2018, equation (1)) at the equator to drive fast magnetosonic waves. According to Xiao and Feng (2006), the partial shell velocity distribution anywhere along the field line is given by

$$f_s = \frac{n_{s,0}(B_0/B)^{l/2}}{\pi^{3/2}\theta_s^3 C(v_s/\theta_s)} e^{-(v-v_s)^2/\theta_s^2}\sin^l\alpha, \quad (11)$$

where $n_{s,0}$ is the number density at the equator, v_s is the shell speed, θ_s is the thermal spread of the shell, and

$$C(b) = \left[be^{-b^2} + \sqrt{\pi}\left(\frac{1}{2} + b^2\right)\mathrm{erfc}(-b)\right]\frac{\Gamma(1+l/2)}{\Gamma(1.5+l/2)}. \quad (12)$$

Here $\mathrm{erfc}(x)$ is the complementary error function and $\Gamma(x)$ is the gamma function. Note that v_s, θ_s, and l are invariant along a field line (thus dropping subscript 0), but the density is given by $n_s = n_{s,0}(B_0/B)^{l/2}$. The Maxwellian distribution is recovered when $l = v_s = 0$.

Equation (11) does not in general ensure a magnetohydrodynamics (MHD) equilibrium when spatial variations other than those in the parallel direction are considered (Hu & Denton, 2009). To ensure pressure balance, one may use the approach of Hu et al. (2010) to initialize simulation particles and the background magnetic field. There, an anisotropic MHD model is solved to obtain the total particle pressure and the magnetic field that are in equilibrium. Then the initial background magnetic field is the magnetic field from the MHD solution. The pressure from the MHD solution is assigned to each particle population to load simulation particles accordingly. (See Hu et al., 2010, section 2.3 for details.) This will be implemented in a future iteration.

3. Initial Setup and Local Instability Analysis

The simulation domain is centered at the reference field line. The wave event presented by Min et al. (2018) is used to select the necessary parameters. Because the wave length of the fast magnetosonic mode is typically scaled by the proton inertial length $\lambda_p = c/\omega_{pp}$, the ratio of $r_{0,\mathrm{ref}}$ to λ_p is an important parameter determining the size of the simulation domain and the inhomogeneity of the dipole magnetic field. The observations showed that the maximum wave power occurred at a radial distance of about 5.6 R_E and near the magnetic equator, where $R_E \approx 6378$ km is the Earth's radius. Also from the observed total plasma number density of $n_0 = 24\ \mathrm{cm}^{-3}$, the proton inertial length is $\lambda_p \approx 0.00727 R_E$. Therefore, the realistic ratio is $r_{0,\mathrm{ref}}/\lambda_p \approx 770$. The

present simulations, however, use a ratio 1.5 times smaller (i.e., $r_{0,\mathrm{ref}}/\lambda_p = 513.3$) so that fewer grid points can be used to represent the same range of magnetic field magnitudes relative to the reference value. Tests suggest that $\Delta_2 = 0.05\lambda_p$ with 960 grid points in the q^2 coordinate direction is sufficient to resolve a wide wave number spectrum of the fast magnetosonic mode (see next paragraph for plasma parameters). The background magnetic field strength at the inner and outer boundaries are $1.16B_{0,\mathrm{ref}}$ and $0.877B_{0,\mathrm{ref}}$, respectively. If the same number density (or equivalently inertial length) as the observations is assumed, the reference field line is at 3.7 R_E and the length of the simulation domain is about 0.35 R_E. This situation may occur during disturbed geomagnetic conditions when the plasmapause has been pushed inward and additionally, fresh injections have provided free energy.

Min et al. (2018) showed that fast magnetosonic waves observed by the Van Allen Probes were driven by a tenuous partial shell distribution of energetic protons with $n_{s,0}/n_0 = 0.05$, $l = 1$, $v_s = 1.7v_{A,ref}$, and $\theta_s^2 = 0.185v_{A,\mathrm{ref}}^2$, where $v_{A,\mathrm{ref}}$ denotes the Alfvén speed at the reference field line. We simulate fast magnetosonic waves using the same partial shell distribution. But we use a single Maxwellian to represent the remaining 95% of protons for simplicity. At first, the background protons have small but finite temperature so that the plasma beta of this Maxwellian population is $\beta_b = 0.00475$. As will be shown, the corresponding temperature is sufficiently small that the cold plasma extraordinary mode dispersion relation provides a good approximation. Later, we increase β_b by a factor of 10 to investigate the warm plasma effects on the evolution of the fast magnetosonic mode. The last species is the charge-neutralizing electrons with $\beta_e = 0.005$. We assume that this three-component plasma is uniformly distributed in the simulation domain (across q^2) for simplicity. To facilitate the computations, we use a reduced ratio of the proton to electron mass, $m_p/m_e = 100$, and a reduced ratio of the light to Alfvén speed, $c/v_{A,\mathrm{ref}} = 30$. The integration time step is $\Delta t\Omega_{p,\mathrm{ref}} = 0.001$, where $\Omega_{p,\mathrm{ref}}$ is the proton cyclotron frequency at the center of the simulation domain. The number of simulation particles per cell is 100,000 for the partial shell protons, and 50,000 for the background protons and electrons, respectively. The number of wave masking grid points is 30 (corresponding roughly to one inertial length) at both boundaries with $r_d = 0.2$ and $r_r = 1$. The simulations were run using 32 cpu cores and the simulation with the longest time evolution took about 22 days.

Linear kinetic dispersion relations (Min et al., 2018) are solved for complex frequencies at $k_{\|} = 0$ using the local quantities measured at both boundaries and at the center. Figure 2 shows the results for the case with cooler background protons. Overall, the real part of the solutions closely follows the cold plasma extraordinary dispersion relation, indicating that the cold plasma approximation may be appropriate to describe the dispersion properties of the fast magnetosonic mode for the parameters assumed. But deviations start to appear as the frequency gets close to the lower hybrid frequency, $\omega_{lh} = \Omega_p/\sqrt{v_A^2/c^2 + m_e/m_p}$, where Ω_p is the local proton cyclotron frequency and the local Alfvén speed is $v_A/v_{A,\mathrm{ref}} = B/B_{0,\mathrm{ref}}$ for the present case (uniform density). Note also that ω_{lh}/Ω_p varies over the simulation domain ($\omega_{lh}/\Omega_p = 9.33$, 9.49, and 9.60 at the inner boundary, at the center, and at the outer boundary, respectively), leading to a variation in the wave numbers where the high-frequency unstable modes appear.

The third harmonic mode appears to be stable near the inner boundary but becomes unstable somewhere between the inner boundary and the center region. (The harmonic is defined in terms of Ω_p.) This can be explained as follows. Although the absolute ring/shell speed and the thermal spread of the partial shell are held constant over the simulation domain, the values relative to v_A are an increasing function of the radial distance since $v_A/v_{A,\mathrm{ref}} = B/B_{0,\mathrm{ref}}$ for the present setup. According to Boardsen et al. (1992), Horne et al. (2000), and Chen et al. (2010), the larger the ring/shell speed relative to local v_A, the smaller the harmonic number where the instability can grow. Finally, the maximum growth rate normalized to Ω_p decreases with q^2 (or radial distance). This means that the decrease of the maximum growth rate normalized to $\Omega_{p,\mathrm{ref}}$ with respect to the radial distance is even greater. It is important to note that there is no appreciable damping in between the harmonics. Therefore, as far as the propagation exactly perpendicular to **B** is concerned, the fast magnetosonic mode will experience little damping once it leaves the source region.

Figure 3 shows the linear theory results for the case with warmer background protons at the inner and outer boundaries. Apparently, the cold plasma dispersion relation (blue dashed curves) is no longer valid at least for $\omega_r/\Omega_p \gtrsim 5$. Instead, the MHD dispersion relation with thermal correction (blue solid curves) better represents the increased phase speed of the kinetic solutions. The MHD dispersion relation at propagation perpendicular to the background magnetic field (e.g., K. Liu, 2007, equation (2.89)) is given by $\omega^2/k_\perp^2 = c_s^2 + v_A^2/Q$, where $c_s = \sqrt{(5/3)\beta_b}v_A$ is the sound speed and $Q = 1 + (m_e/m_p)k_\perp^2\lambda_p^2$. Therefore, the phase speed is an increasing

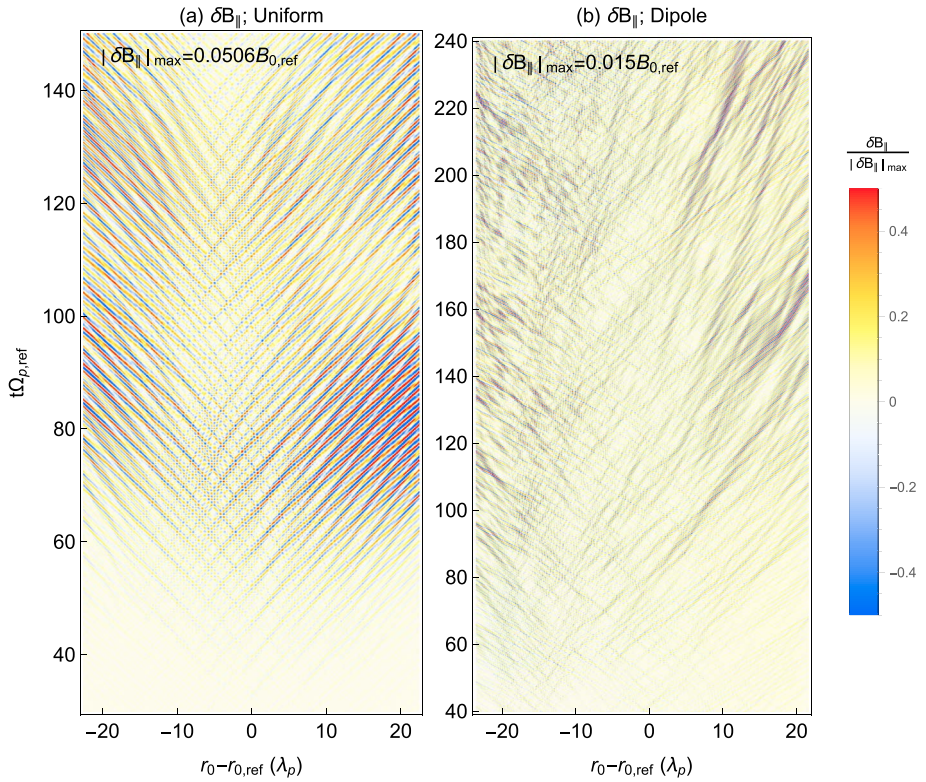

Figure 4. Compressional component ($\delta B_{\parallel}$) of the fluctuating magnetic field as a function of time and radial distance in the (a) uniform and (b) dipole background magnetic fields. The color scale represents $\delta B_{\parallel}$ normalized to the maximum value, which is labeled in each panel.

function of $\sqrt{\beta_b}$. The instability appears to cease as one moves outward; the solutions at the center region did not show any positive instability growth (not shown). It is worth noting from Figure 3b that the dispersion curves immediately above and below are no longer connected at the integer harmonic frequency. In fact, the separation of the curves increases with the temperature. The same is true without the partial shell component, in which case there are no growing modes (not shown). This indicates that wave propagation may be affected when the normalized frequency reaches one of the integer harmonics.

4. Simulation Results

First, we present the simulation results for the case with cooler background protons. For comparison, a simulation with a uniform background magnetic field is also carried out. For this, we simply set $r_{0,\mathrm{ref}}/\lambda_p = 10^6$ (sufficiently large so that the background magnetic field is essentially uniform within the simulation domain) but otherwise kept all other parameters identical. Figure 4 shows a side-by-side comparison of the compressional component ($\delta B_{\parallel}$) of the fluctuating magnetic field as a function of time and radial distance for the two simulations. (The masking regions where the outgoing waves are absorbed are located outside of the plot.) Note that the time scale is different. The simulations were terminated at $t\Omega_{p,\mathrm{ref}} = 150$ and 300 for the uniform and dipole cases, respectively. The very different time scale of the evolution may be explained as follows. There is roughly the same amount of free energy in both systems, but radial propagation in the dipole magnetic field (Figure 4b) quickly removes the waves from the region where they can grow (that is, where their frequency becomes harmonics of Ω_p). Consequently, it takes much longer to use up the free energy in the dipole system. (Later in this section, the time scale for wave amplification will be shown.) At first glance, the radial gradient clearly introduces asymmetry between the inward and outward traveling waves and results in a more complex pattern of propagation. In addition, wave enhancement appears slightly earlier near the inner boundary and subsequently extends toward the outer boundary. This feature appears to be consistent with the local instability growth where the growth rate is an increasing function of the background magnetic field strength (see Figure 2 and related discussion in section 3).

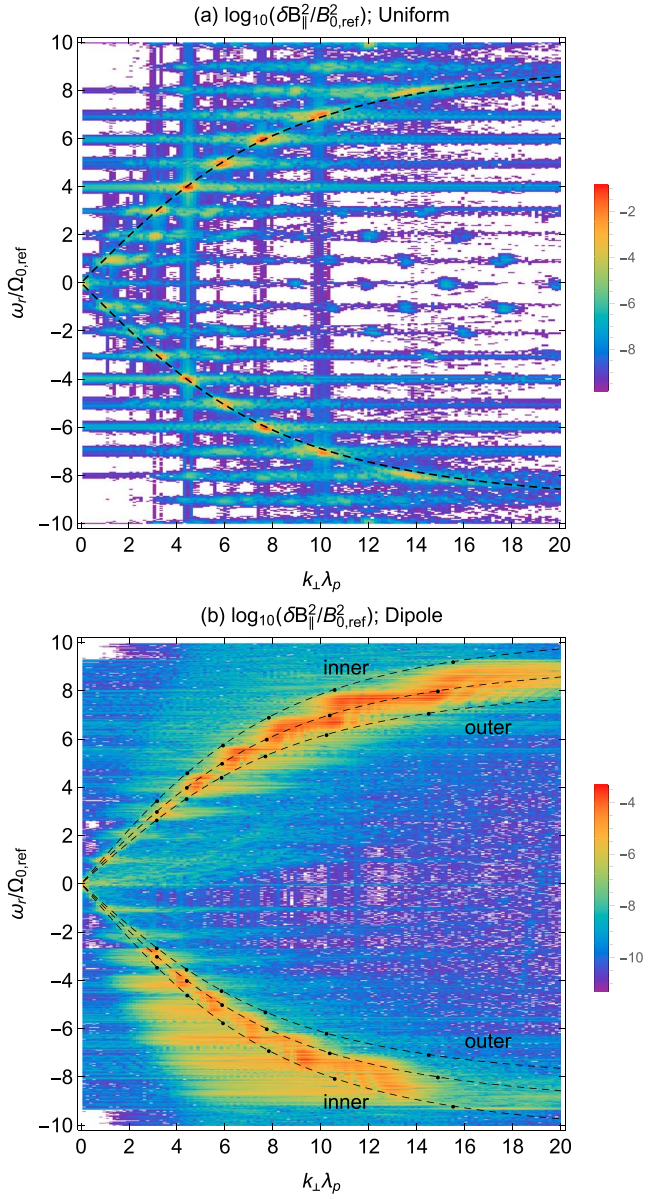

Figure 5. Frequency-wave number spectrum of $\delta B_{\parallel}$ corresponding to Figure 4 using the entire time series and spatial domain excluding the masking region. The positive (negative) frequency region corresponds to outward (inward) propagating modes. In panel (a), the dashed curve is the cold plasma extraordinary mode dispersion relation. In panel (b), the three dashed curves are the cold plasma dispersion relations at the inner boundary (left), at the center of the domain (middle), and at the outer boundary (right), respectively. The tiny dots are placed on the curves to indicate harmonic numbers from 3 to 8 on those locations. The lower hybrid frequencies at the inner boundary, at the center, and at the outer boundary are $\omega_{lh}/\Omega_{p,\mathrm{ref}} = 10.75$, 9.49, and 8.48, respectively.

The entire time series and spatial domain (excluding the masking region) of $\delta B_{\parallel}$ is used to perform a fast Fourier transform (FFT). A hamming window function is applied prior to the FFT. Figure 5 shows the frequency-wave number power spectrograms corresponding to Figure 4. The cold plasma extraordinary mode dispersion relations at the boundaries and the center of the simulation domain are superimposed with the dashed curves. In addition, for the dipole case, tiny dots are placed on the curves to mark the harmonic numbers from 3 to 8. (Only the dots on the middle curve line up with integer values of $\omega_r/\Omega_{p,\mathrm{ref}}$.) The negative and positive frequency regions correspond to waves propagating radially inward and outward, respectively. In the uniform case, the enhancement occurs at exact harmonics and closely follows the cold plasma dispersion relation. This is exactly what is expected from the linear theory analysis. For the dipole case, the enhancement

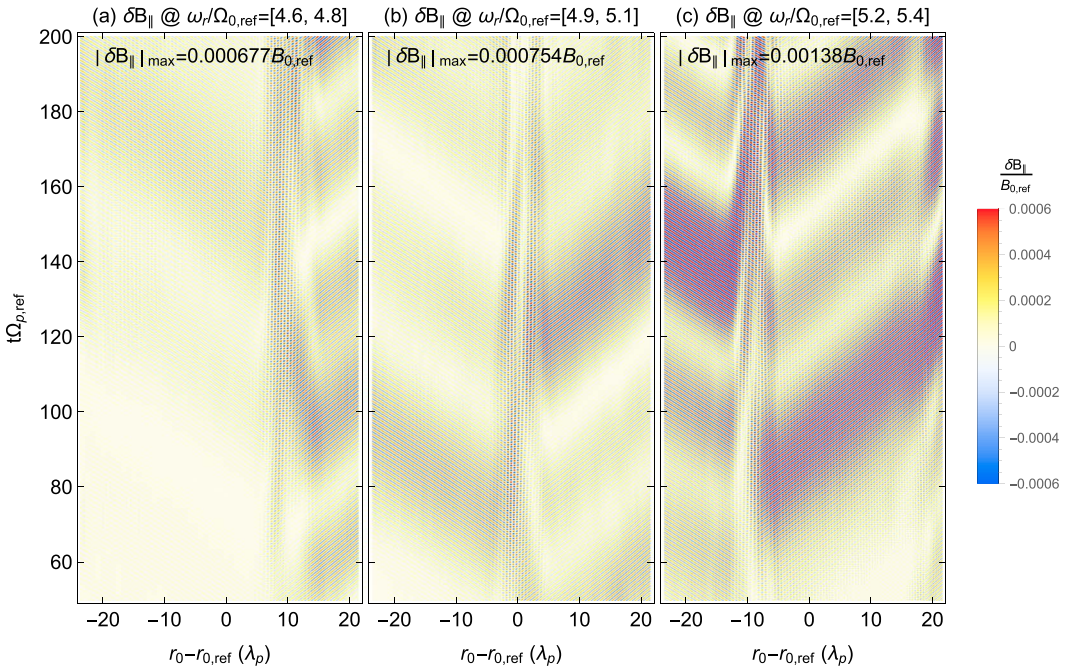

Figure 6. Compressional component ($\delta B_{\parallel}$) of the fluctuating magnetic field in the dipole case filtered in the frequency ranges as labeled.

is bounded by the two outermost dispersion curves. This is an expected result because we know from the uniform case that the excited waves should closely follow the cold plasma dispersion relation. [The leakage of spectral power to smaller $k_{\perp}$ (inward of the inner boundary) in the $\omega_r < 0$ region may be caused by the FFT on nonperiodic data.]

The horizontal striations of the enhanced power in Figure 5b suggest that the frequency is indeed conserved as the waves propagate from the source region. For example, by looking at the fourth harmonic mode excited from near the inner boundary ($\omega_r \approx 4.5\Omega_{p,\mathrm{ref}}$) and propagating radially outward ($\omega_r > 0$ region), the enhanced power is stretched all the way to the outer dispersion curve where the frequency roughly corresponds to the fifth harmonic number there. Because the frequency normalized to Ω_p barely traveled one harmonic number and because there should be no wave growth in between these two harmonic numbers according to the local instability analysis, the fourth harmonic mode excited near the inner boundary region should be the sole contributor to this particular frequency (with sign). The same logic can be applied to the waves propagating inward. The L-shaped boundary of power for $\omega_r < 0$ near the outer boundary and the left-right-reflected L-shaped boundary of power for $\omega_r > 0$ near the inner boundary is the evidence that wave growth is absent in between the harmonics.

It is as though a particular frequency is tuned to a particular location or locations in space. This may allow us to better understand the source region and how the excited wave emanates from it by picking out a particular frequency. The procedure is as follows: The simulated $\delta B_{\parallel}$ at each point in space is transformed into frequency space, the transformed data are then band-pass filtered to a narrow frequency band of $0.2\Omega_{p,\mathrm{ref}}$ in the vicinity of the tuning frequency, and finally, the masked data are transformed back to real space. Apparently, all integer values of $\omega_r/\Omega_{p,\mathrm{ref}}$ should correspond to the location at $r_0 = r_{0,\mathrm{ref}}$. And the values slightly below and above should be mapped to the regions of $r_0 > r_{0,\mathrm{ref}}$ and $r_0 < r_{0,\mathrm{ref}}$, respectively. This is indeed what is shown in Figure 6, where we tuned to $\omega_r/\Omega_{p,\mathrm{ref}} = 4.7$, 5, and 5.3. It is easy to locate the source location(s) by looking at the wave propagation pattern. The source region is finite ($\Delta r_0 \lesssim 5\lambda_p$) because of the finite frequency width that we used for the frequency filtering and perhaps because the growth rate also has a finite frequency width (Figure 2). Figure 6c is an example of two source locations. The first is at $r_0 - r_{0,\mathrm{ref}} \approx -10\lambda_p$ corresponding to $\omega_r/\Omega_p = 5$ and the second is at $r_0 - r_{0,\mathrm{ref}} \approx 20\lambda_p$ corresponding to $\omega_r/\Omega_p = 6$. (Inward propagation from the second source is not clearly seen due perhaps to the smaller growth rate and/or the close proximity to the simulation boundary.)

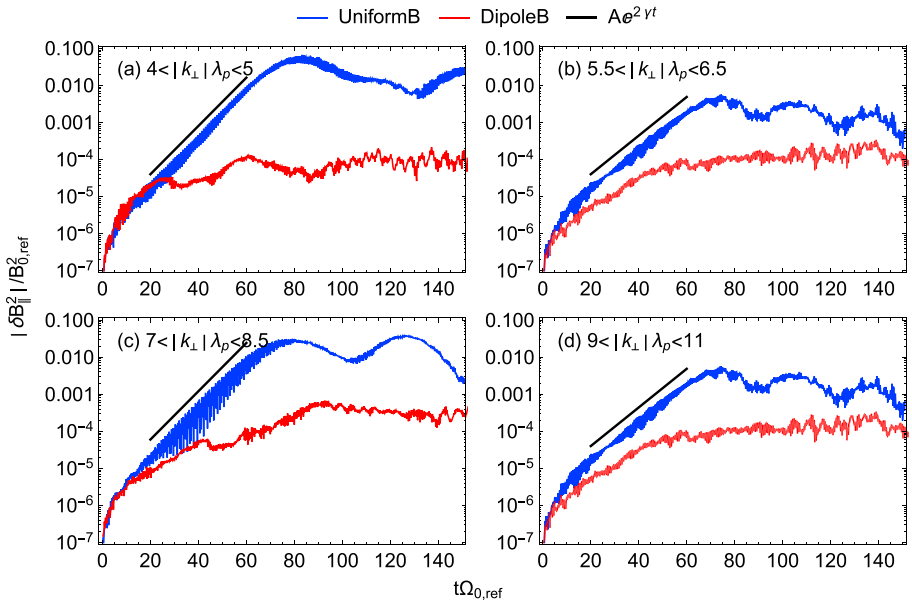

Figure 7. Comparison of the time scales of wave amplification between the uniform and dipole cases with cooler background protons. Each panel shows the power of $\delta B_{\parallel}$ integrated within the wave number range as labeled. The wave number ranges, (a) $4 \le |k_{\perp}|\lambda_p \le 5$, (b) $5.5 \le |k_{\perp}|\lambda_p \le 6.5$, (c) $7 \le |k_{\perp}|\lambda_p \le 8.5$, and (d) $9 \le |k_{\perp}|\lambda_p \le 11$, represent the harmonic modes from 4 and 7, respectively (Figure 5). The blue and red curves are for the integrated power from the uniform and dipole cases, respectively, and the black solid lines represent approximate fits to the linear growth phases of the uniform case. The estimated growth rates are $\gamma_{est} \approx 0.075$, 0.06, 0.075, and $0.07\Omega_{0,ref}$ from the fourth to seventh harmonic modes, respectively.

Figure 7 compares the time scales of wave amplification between the uniform and dipole cases. We chose the harmonic modes from 4 and 7 for the comparison. For the uniform case (Figure 5a), these harmonic modes are well contained within the following wave number ranges: $4 \le |k_{\perp}|\lambda_p \le 5$, $5.5 \le |k_{\perp}|\lambda_p \le 6.5$, $7 \le |k_{\perp}|\lambda_p \le 8.5$, and $9 \le |k_{\perp}|\lambda_p \le 11$, respectively. For the dipole case (Figure 5b), however, it is hard to isolate these harmonic modes. But we still use the same wave number ranges to represent the corresponding harmonic modes, understanding that, on the one hand, the given harmonic mode can stretch outside the wave number range specified, and on the other hand, the adjacent harmonic modes can also pollute the harmonic mode of interest. We Fourier transform $\delta B_{\parallel}$ in space at every time step and add all the power within the wave number ranges mentioned above. Propagation in both directions is taken into account in the calculation. For each harmonic mode, the linear growth rate for the uniform case is estimated as shown with the black solid lines. The estimated growth rates are $\gamma_{est} \approx 0.075$, 0.06, 0.075, and $0.07\Omega_{0,ref}$ from the fourth to seventh harmonic modes, respectively. In comparison, the corresponding maximum growth rates from linear theory at the center (Figure 2b) are $\gamma_{lin} = 0.087$, 0.08, 0.081, and $0.075\Omega_{0,ref}$, respectively, which are in qualitative agreement with the simulation results. In comparison with the uniform case, the growth rates are smaller, the saturation levels are lower, and the linear phase of wave amplification is less clear for the dipole case. We attribute this to the ineffective amplification of the fast magnetosonic mode during radial propagation, as discussed earlier.

Figure 8 shows the frequency power spectra of $\delta B_{\parallel}$ in the simulations with the uniform and dipole magnetic fields, respectively. For the dipole case, $\delta B_{\parallel}$ is sampled near the center region. Comparing with the uniform case, superposition of the waves from multiple sources clearly smooths out the discrete harmonic peaks. According to Chen et al. (2016), the minimum radial extent of the source region that results in a continuous, broadband frequency spectrum is related to the harmonic number, $\Delta r_0/r_0 = 1/(3j)$, for the dipole magnetic field, where Δr_0 is the radial extent of the source region and $j = \omega_r/\Omega_p$. Using values of $\Delta r_0 \approx 45\lambda_p$ and $r_0 = 513.3\lambda_p$, we get $\omega_r/\Omega_p \approx 3.8$. Consistent with this estimation, the distance in frequency space between two dots (marking the local harmonics of Ω_p) at the innermost and outermost dispersion curves shown in Figure 5b becomes Ω_p approximately at the fourth harmonic frequency. Now looking at Figure 8, it appears to be indeed the fourth harmonic frequency that divides the continuous spectrum from the discrete one for the present simulation setup; the third harmonic mode clearly exhibits an isolated peak, whereas fifth

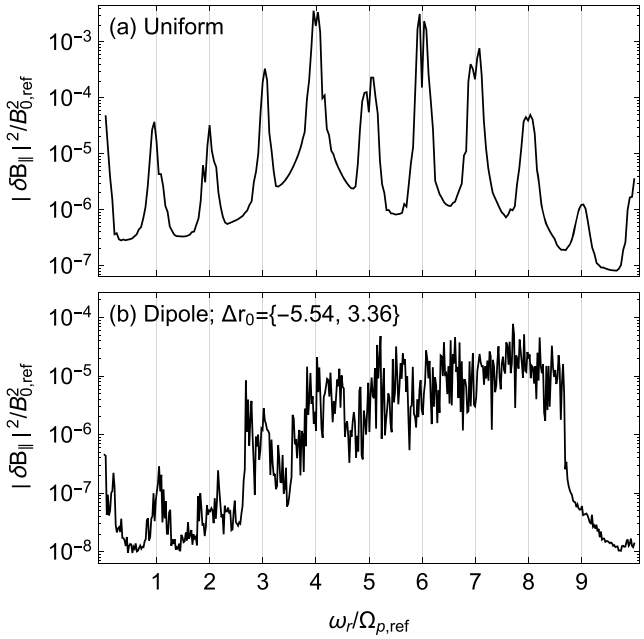

Figure 8. Comparison of frequency power spectra of $\delta B_{\parallel}$ for the simulations with (a) uniform and (b) dipole magnetic fields. For the dipole case, $\delta B_{\parallel}$ is sampled near the center region.

harmonic and above are broadbanded. Figure 8 supports the idea that a broadband frequency spectrum from observations may result from radial propagation (Chen et al., 2016; Perraut et al., 1982; Posch et al., 2015). On the other hand, it is worth noting that Chen et al. (2016) showed that local instability can also produce a broadband spectrum when the growth rate is sufficiently large. In addition, Shklyar and Balikhin (2017) suggested that wave amplification during radial propagation can reproduce the wave phenomenon reported by Balikhin et al. (2015) where the spectral intensity below exact cyclotron harmonics is much higher than above.

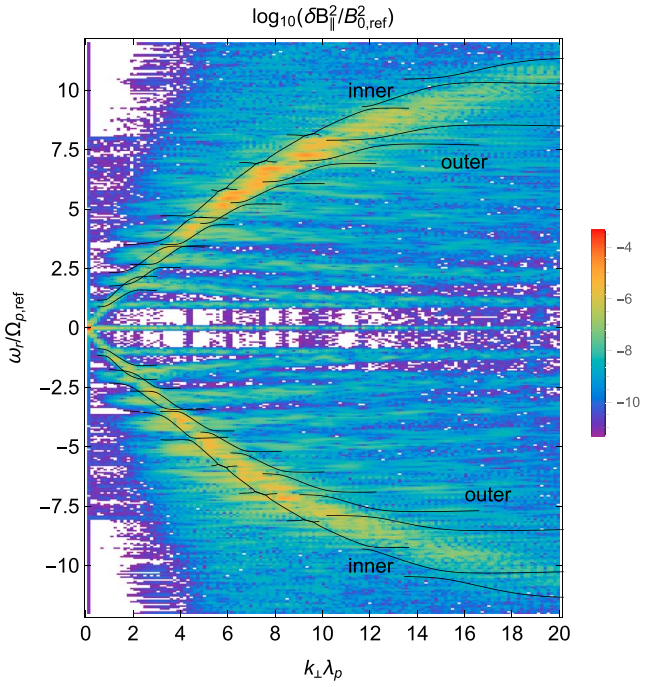

Figure 9. Frequency-wave number spectrum of $\delta B_{\parallel}$ corresponding to the simulation with warmer background protons. The real parts of the linear theory solutions at the inner (left) and outer (right) boundaries shown in Figure 3 are superimposed.

We only briefly show the simulation results for the case with warmer background protons because of the low saturation level of the fast magnetosonic mode. Figure 9 shows the frequency-wave number spectrogram of the simulated $\delta B_{\parallel}$. The aperiodic ($\omega_r = 0$) mode, which is most likely caused by the pressure imbalance that our simulation does not enforce initially, dominates because of the relatively low amplitudes of the fast magnetosonic mode. However, the enhanced power of the fast magnetosonic mode is clearly bound by the warm plasma dispersion curves at the boundaries and the horizontal striations are also seen.

To better understand the effects of warm plasma wave dispersion on wave propagation, we pump a prescribed wave into the system, similar to X. Liu et al. (2018). We also remove the partial shell component to suppress the self-consistent wave excitation. To highlight wave absorption at harmonic(s) of Ω_p and consequent proton heating, we present one representative case, where a wave with frequency $\omega_r = 7.31\Omega_{p,\mathrm{ref}}$ (between sixth and seventh harmonic) was pumped at $r_0 - r_{0,\mathrm{ref}} = -20\lambda_p$ for about $t\Omega_{p,\mathrm{ref}} = 50$. (We obtained similar results for combinations of $\omega_r/\Omega_p \approx 4.5$ and 6.5 and $r_0 - r_{0,\mathrm{ref}} = \pm 20\lambda_p$.) Figure 10 shows the spatiotemporal evolution of wave energy in the cases with the cool ($\beta_b = 0.005$) and warm ($\beta_b = 0.05$) proton populations. While no damping is seen in the cooler plasma as the waves propagate to larger r_0, there is clear absorption of wave energy in the warmer plasma near the location where the wave frequency matches the seventh harmonic at $r_0 - r_{0,\mathrm{ref}} = -7.5\lambda_p$. The partially

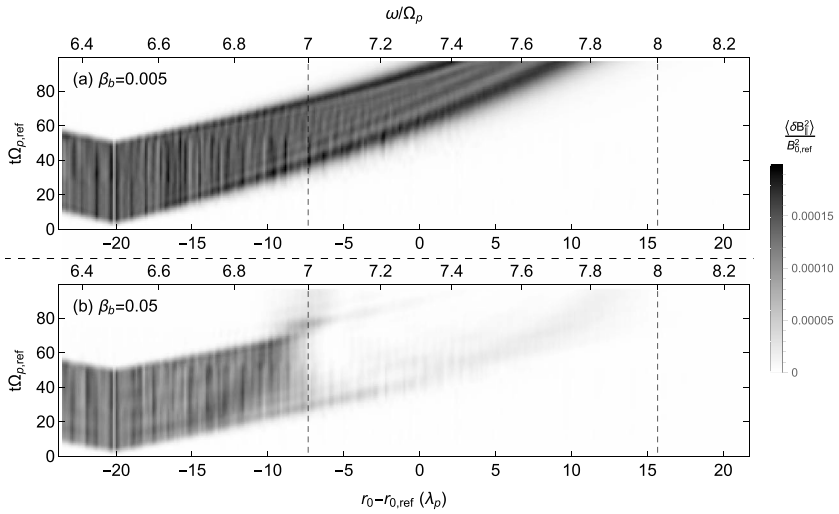

Figure 10. Propagation of wave energy ($|\delta B_{\parallel}|^2$) pumped at $r_0 - r_{0,\mathrm{ref}} = -20\lambda_p$ with $\omega_r = 7.31\Omega_{p,\mathrm{ref}}$ in the cool (a: $\beta_b = 0.005$) and warm (b: $\beta_b = 0.05$) plasmas. The top horizontal axes denote ω_r normalized to the local proton cyclotron frequency, Ω_p. The two vertical dashed lines are drawn at the seventh and eighth harmonics.

transmitted wave appears to reach the eighth harmonic near $r_0 - r_{0,\mathrm{ref}} = 15\lambda_p$, but it is not clear from this simulation whether the absorption also occurs there. Corresponding to the wave energy, Figure 11 shows the azimuthal component of proton kinetic energy normalized to the initial value. The azimuthal component is chosen to diagnose the perpendicular heating because the sloshing motion of background protons—a linear response to the pumping wave—occurs predominantly in the direction of spatial variation (i.e., radial direction for the present case) (e.g., Sun et al., 2017, Figure 9). Corresponding to the wave absorption, the heating appears to occur near the seventh harmonic at $t\Omega_{p,\mathrm{ref}} \gtrsim 40$ in the warmer plasma. A much weaker signal of heating is also visible near the seventh harmonic in the cooler plasma, although the wave absorption was hard to identify from Figure 10a.

Figure 12 shows the wave and particle energies for the driven simulations in Figures 10 and 11. First, we describe the energy evolution of the case with the cooler plasma. Figure 12a shows the wave energy (blue), particle kinetic energy (red), and the total energy (black). (The initial value is subtracted from the particle kinetic energy). All curves start to increase from $t\Omega_{0,\mathrm{ref}} = 3$ when we started pumping the wave. The increase rate is then reduced by half at about $t\Omega_{0,\mathrm{ref}} = 13$ (first dashed line) when the first wave propagating inward

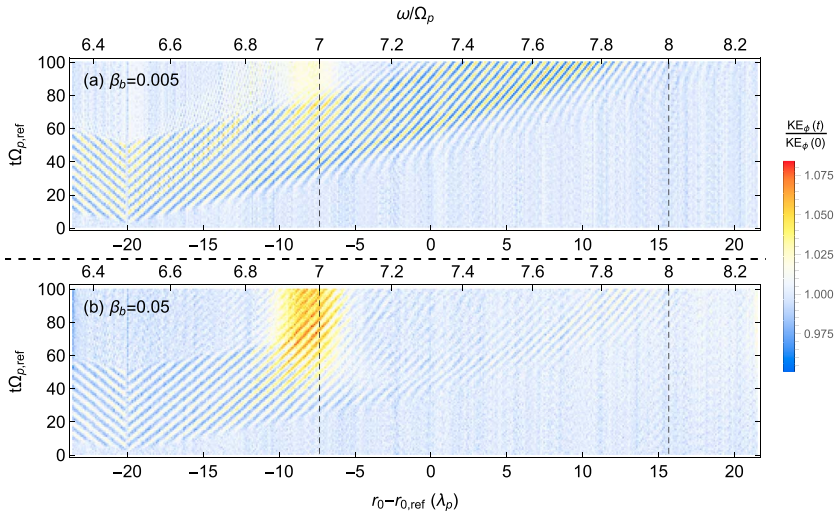

Figure 11. Spatiotemporal evolution of the azimuthal component of proton kinetic energy in response to the pumping wave in Figure 10. The kinetic energy is normalized to the initial value.

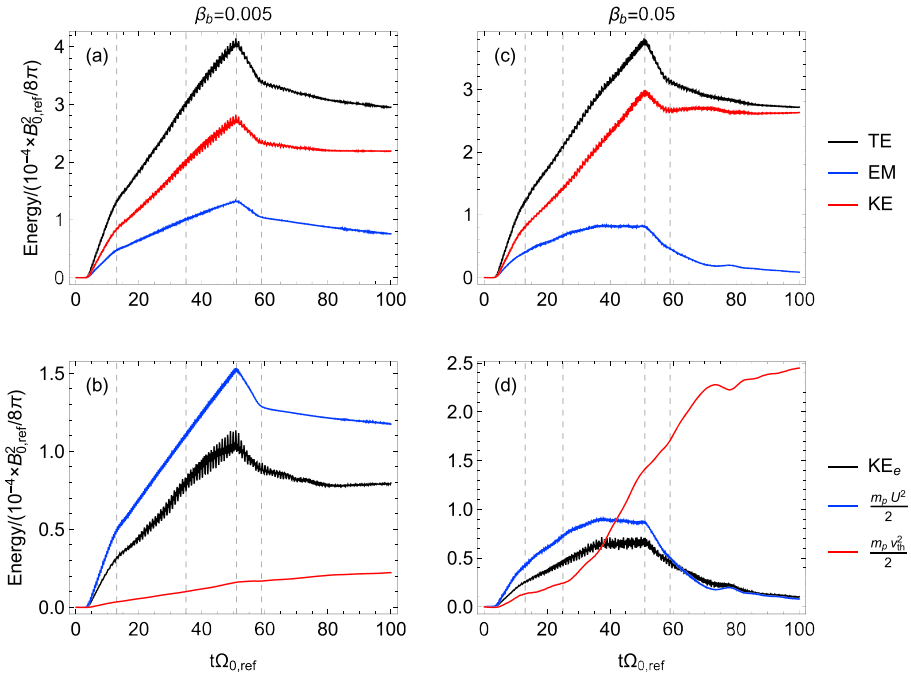

Figure 12. Wave and particle energies for the driven simulations in Figures 10 and 11. Left panels are for $\beta_b = 0.005$ and right panels are for $\beta_b = 0.05$. The lines in the top panels correspond to electromagnetic wave energy (EM, blue), and proton and electron kinetic energy (KE, red), and the total energy (TE, black). The initial value has been subtracted from the particle kinetic energy. The lines in the bottom panels correspond to electron kinetic energy (KE$_e$, black), proton bulk flow energy ($m_p U^2/2$, blue), and proton thermal energy ($m_p v_{th}^2/2$, red). Again, the initial values have been subtracted from the electron kinetic energy and proton thermal energy. Each energy is spatially averaged and divided by $10^{-4}B^2_{0,ref}/8\pi$.

has reached the inner boundary. The energy curves continue to climb up at a reduced rate until the external current source has been turned off at about $t\Omega_{0,ref} = 51$ (third dashed line). Note that the first wave reached the seventh harmonic mark at about $t\Omega_{0,ref} = 35$ (second dashed line). After the external source of energy is turned off, the energy curves exhibit a steep decline until about $t\Omega_{0,ref} = 59$ (last dashed line) when the last wave propagating inward has reached the inner boundary. Note that the total energy gradually decreases afterward even though the wave propagating outward has not reached the outer boundary; this is because the system continuously loses energy through the absorbing boundaries. The evolution of the wave and particle energy is very similar, and the particle energy increase is about twice that of the wave energy. Figure 12b shows the electron kinetic energy (black), the proton bulk flow energy (due to the sloshing motion; blue), and the proton thermal energy (red). (Again, the initial values are subtracted from the electron kinetic and proton thermal energy.) Apparently, the sloshing motion of protons dominates the proton kinetic energy. (The same is true for electrons). The thermal heating of protons is minor, but unlike the bulk flow energy, the thermal energy continuously increases (perhaps corresponding to the heating signature in Figure 11a near the seventh harmonic mark).

Now we describe the energy evolution for the case with the warmer plasma. Figure 12c shows the wave energy, particle kinetic energy, and the total energy. All but the second vertical dashed line mark the same temporal locations as those in Figure 12a. For this case, the first wave reached the seventh harmonic mark at about $t\Omega_{0,ref} = 25$ indicated by the second dashed line. Whereas the particle energy has a trend quite similar to that of the cooler plasma, the wave energy, unlike the previous case, exhibits a plateau between $t\Omega_{0,ref} = 35$ and 51. Looking at Figure 12d, this period corresponds to a rapid increase of the thermal energy of protons, which surpassed the bulk flow energy at about $t\Omega_{0,ref} = 41$. Note that the rapid increase of the thermal energy actually started when the first wave reached the seventh harmonic mark (second dashed line). The protons were heated further until the total energy curve flattened out after about $t\Omega_{0,ref} = 70$, approximately when the last wave reached the seventh harmonic mark (Figure 10b). This is the evidence that the reddish blob in Figure 11b is indeed the result of heating by wave absorption at the seventh harmonic. In contrast,

the evolution of the proton bulk flow energy and the electron kinetic energy is very similar to that of the wave energy, an indication of the linear response to the pumping wave.

5. Summary and Discussions

A new electromagnetic PIC code has been developed to investigate self-consistent evolution of the fast magnetosonic mode in a dipole magnetic field. As a first step, we examined the case of one-dimensional variation in the radial direction at the magnetic equator, thus taking into account the radial gradient of the dipole magnetic field. The wave event studied by Min et al. (2018) was used to derive the simulation parameters. We used a simulation scale size reduced by a factor of 1.5 to facilitate the computations. This means that if the plasma density is the same as the observed value, the L shell of the center of the simulation domain corresponds to 3.7 R_E; this may occur during disturbed geomagnetic conditions when the plasmapause has been pushed inward. The free energy source that drives the fast magnetosonic waves was determined from the observations. Min et al. (2018) showed that a tenuous (5%) partial shell distribution of energetic protons with a ring/shell speed at 1.7 times the Alfvén speed was the source of free energy. A single Maxwellian was used to represent the remaining protons for simplicity. Two cases were considered, one with cool temperature ($\beta_b \approx 0.005$) and another with warm temperature ($\beta_b \approx 0.05$). Both the free energy source and the background protons were uniformly distributed. As a result, the wave excitation was not localized in space and the effects of the plasma density gradient such as trapping (e.g., X. Liu et al., 2018; Ma, Li, Chen, Thorne, Kletzing, et al., 2014) were not taken into account.

Our main findings are as follows. (1) Linear theory showed that increased background plasma temperature has two effects. First, the phase speed of the fast magnetosonic mode increases due to the increasing contribution from the sound speed; and second, the dispersion curves immediately above and below the integer harmonics separate. (2) Consistent with the prediction of linear theory, the wave excitation only occurred at exact harmonics of the local proton cyclotron frequency, Ω_p. Because of the magnetic field gradient, the absolute frequencies corresponding to the exact harmonic numbers continuously varied with the radial distance. Consequently, the time scale of wave amplification got much longer than that predicted by linear theory and radial propagation from multiple sources led to a broad frequency spectrum of the fast magnetosonic waves observed at a single location. (3) Wave energy propagating in the warmer plasma was absorbed when the wave frequency normalized to Ω_p reached an integer value, where the separation of the dispersion curves occurs. This energy was converted to thermal motion of background protons in the direction perpendicular to the background magnetic field.

The present results set the stage for further investigations of the fast magnetosonic mode beyond the 1-D configuration of the present simulations. In fact, a more effective way to amplify a fast magnetosonic mode is to allow propagation in the azimuthal direction, for which the background magnetic field and thus the normalized frequency remain constant (Boardsen et al., 2016). On the other hand, the inhomogeneity of the background magnetic field (and the plasma density) in general prevents the wave from staying on this optimal path (Chen & Thorne, 2012). Therefore, an immediate next step may be to allow azimuthal variation in addition to the radial variation. This may explain why the observed electric field associated with the fast magnetosonic mode outside the plasmapause is preferentially polarized in the azimuthal direction (Němec et al., 2013).

Acknowledgments
K. Min is grateful to Xueyi Wang for helpful discussions. Data sets used to produce figures are available in a Zenodo data repository at https://doi.org/10.5281/zenodo.1316907. This work was completed in part with resources provided by the Auburn University Hopper Cluster. This work was supported by JHU/APL subcontract FundingNumber937836 to the New Jersey Institute of Technology under NASA prime contract NAS5-01072, NASA grant NNX16AM98G, and NSF grants AGS-1602388 and AGS-1602469. K. Liu's work at Auburn University was also supported by NASA grant NNX17AI52G.

References

Bagdonat, T., & Motschmann, U. (2002). 3D hybrid simulation code using curvilinear coordinates. *Journal of Computational Physics*, *183*, 470–485. https://doi.org/10.1006/jcph.2002.7203

Balikhin, M. A., Shprits, Y. Y., Walker, S. N., Chen, L., Cornilleau-Wehrlin, N., Dandouras, I., et al. (2015). Observations of discrete harmonics emerging from equatorial noise. *Nature Communications*, *6*, 7703. https://doi.org/10.1038/ncomms8703

Boardsen, S. A., Gallagher, D. L., Gurnett, D. A., Peterson, W. K., & Green, J. L. (1992). Funnel-shaped, low-frequency equatorial waves. *Journal of Geophysical Research*, *97*, 14,967–14,976. https://doi.org/10.1029/92JA00827

Boardsen, S. A., Hospodarsky, G. B., Kletzing, C. A., Engebretson, M. J., Pfaff, R. F., Wygant, J. R., et al. (2016). Survey of the frequency dependent latitudinal distribution of the fast magnetosonic wave mode from Van Allen Probes electric and magnetic field instrument and integrated science waveform receiver plasma wave analysis. *Journal of Geophysical Research: Space Physics*, *121*, 2902–2921. https://doi.org/10.1002/2015JA021844

Chan, A. A., Xia, M., & Chen, L. (1994). Anisotropic Alfven-ballooning modes in Earth's magnetosphere. *Journal of Geophysical Research*, *99*, 17,351–17,366. https://doi.org/10.1029/93JA03353

Chen, L., Sun, J., Lu, Q., Gao, X., Xia, Z., & Zhima, Z. (2016). Generation of magnetosonic waves over a continuous spectrum. *Journal of Geophysical Research: Space Physics*, *121*, 1137–1147. https://doi.org/10.1002/2015JA022089

Chen, L., & Thorne, R. M. (2012). Perpendicular propagation of magnetosonic waves. *Geophysical Research Letters*, *39*, L14102. https://doi.org/10.1029/2012GL052485

Chen, L., Thorne, R. M., Jordanova, V. K., & Horne, R. B. (2010). Global simulation of magnetosonic wave instability in the storm time magnetosphere. *Journal of Geophysical Research*, *115*, A11222. https://doi.org/10.1029/2010JA015707

Danielson, D. A. (1992). *Vectors and Tensors in Engineering and Physics*. Menlo Park, CA: Addison-Wesley.

Eastwood, J. W., Arter, W., Brealey, N. J., & Hockney, R. W. (1995). Body-fitted electromagnetic PIC software for use on parallel computers. *Computer Physics Communications*, *87*, 155–178. https://doi.org/10.1016/0010-4655(94)00165-X

Fu, X., Cowee, M. M., Friedel, R. H., Funsten, H. O., Gary, S. P., & Hospodarsky, G. B. (2014). Whistler anisotropy instabilities as the source of banded chorus: Van Allen Probes observations and particle-in-cell simulations. *Journal of Geophysical Research: Space Physics*, *119*, 8288–8298. https://doi.org/10.1002/2014JA020364

Gary, S. P., Liu, K., & Winske, D. (2011). Whistler anisotropy instability at low electron β: Particle-in-cell simulations. *Physics of Plasmas*, *18*(8), 082902. https://doi.org/10.1063/1.3610378

Gulelmi, A. V., Klaine, B. I., & Potapov, A. S. (1975). Excitation of magnetosonic waves with discrete spectrum in the equatorial vicinity of the plasmapause. *Planetary and Space Science*, *23*, 279–286. https://doi.org/10.1016/0032-0633(75)90133-6

Horne, R. B., Wheeler, G. V., & Alleyne, H. S. C. K. (2000). Proton and electron heating by radially propagating fast magnetosonic waves, *105*, 27,597–27,610. https://doi.org/10.1029/2000JA000018

Hrbáčková, Z., Santolík, O., Němec, F., Macúšová, E., & Cornilleau-Wehrlin, N. (2015). Systematic analysis of occurrence of equatorial noise emissions using 10 years of data from the cluster mission. *Journal of Geophysical Research: Space Physics*, *120*, 1007–1021. https://doi.org/10.1002/2014JA020268

Hu, Y. (2010). Hybrid code simulation of electromagnetic ion cyclotron waves in curvilinear coordinates (Ph.D. thesis), Dartmouth College.

Hu, Y., & Denton, R. E. (2009). Two-dimensional hybrid code simulation of electromagnetic ion cyclotron waves in a dipole magnetic field. *Journal of Geophysical Research*, *114*, A12217. https://doi.org/10.1029/2009JA014570

Hu, Y., Denton, R. E., & Johnson, J. R. (2010). Two-dimensional hybrid code simulation of electromagnetic ion cyclotron waves of multi-ion plasmas in a dipole magnetic field. *Journal of Geophysical Research*, *115*, A09218. https://doi.org/10.1029/2009JA015158

Kasahara, Y., Kenmochi, H., & Kimura, I. (1994). Propagation characteristics of the ELF emissions observed by the satellite Akebono in the magnetic equatorial region. *Radio Science*, *29*, 751–767. https://doi.org/10.1029/94RS00445

Ke, Y., Gao, X., Lu, Q., Wang, X., & Wang, S. (2017). Generation of rising-tone chorus in a two-dimensional mirror field by using the general curvilinear PIC code. *Journal of Geophysical Research: Space Physics*, *122*, 8154–8165. https://doi.org/10.1002/2017JA024178

Laakso, H., Junginger, H., Schmidt, R., Roux, A., & de Villedary, C. (1990). Magnetosonic waves above fc(H+) at geostationary orbit—GEOS 2 results. *Journal of Geophysical Research*, *95*, 10,609–10,621. https://doi.org/10.1029/JA095iA07p10609

Liu, K. (2007). Particle-in-cell simulations of particle energization in the auroral region (Ph.D. thesis), Cornell University.

Liu, X., Chen, L., Yang, L., Xia, Z., & Malaspina, D. M. (2018). One-dimensional full wave simulation of equatorial magnetosonic wave propagation in an inhomogeneous magnetosphere. *Journal of Geophysical Research: Space Physics*, *123*, 587–599. https://doi.org/10.1002/2017JA024336

Liu, K., Gary, S. P., & Winske, D. (2011). Excitation of magnetosonic waves in the terrestrial magnetosphere: Particle-in-cell simulations. *Journal of Geophysical Research*, *116*, A07212. https://doi.org/10.1029/2010JA016372

Liu, K., Seyler, C. E., & Xu, T. (2006). Particle-in-cell simulations of current shear-driven instabilities and the generation of broadband ELF fluctuations. *Journal of Geophysical Research*, *111*, A11307. https://doi.org/10.1029/2006JA011858

Ma, Q., Li, W., Chen, L., Thorne, R. M., & Angelopoulos, V. (2014). Magnetosonic wave excitation by ion ring distributions in the Earth's inner magnetosphere. *Journal of Geophysical Research: Space Physics*, *119*, 844–852. https://doi.org/10.1002/2013JA019591

Ma, Q., Li, W., Chen, L., Thorne, R. M., Kletzing, C. A., Kurth, W. S., et al. (2014). The trapping of equatorial magnetosonic waves in the Earth's outer plasmasphere. *Geophysical Research Letters*, *41*, 6307–6313. https://doi.org/10.1002/2014GL061414

Ma, Q., Li, W., Thorne, R. M., & Angelopoulos, V. (2013). Global distribution of equatorial magnetosonic waves observed by THEMIS. *Geophysical Research Letters*, *40*, 1895–1901. https://doi.org/10.1002/grl.50434

Meredith, N. P., Horne, R. B., & Anderson, R. R. (2008). Survey of magnetosonic waves and proton ring distributions in the Earth's inner magnetosphere. *Journal of Geophysical Research*, *113*, A06213. https://doi.org/10.1029/2007JA012975

Min, K., Liu, K., & Gary, S. P. (2016). Scalings of Alfvén-cyclotron and ion Bernstein instabilities on temperature anisotropy of a ring-like velocity distribution in the inner magnetosphere. *Journal of Geophysical Research: Space Physics*, *121*, 2185–2193. https://doi.org/10.1002/2015JA022134

Min, K., Liu, K., Wang, X., Chen, L., & Denton, R. E. (2018). Fast magnetosonic waves observed by Van Allen Probes: Testing local wave excitation mechanism. *Journal of Geophysical Research: Space Physics*, *123*, 497–512. https://doi.org/10.1002/2017JA024867

Němec, F., Santolík, O., Gereová, K., Macúšová, E., de Conchy, Y., & Cornilleau-Wehrlin, N. (2005). Initial results of a survey of equatorial noise emissions observed by the Cluster spacecraft. *Planetary and Space Science*, *53*, 291–298. https://doi.org/10.1016/j.pss.2004.09.055

Němec, F., Santolík, O., Pickett, J. S., Hrbáčková, Z., & Cornilleau-Wehrlin, N. (2013). Azimuthal directions of equatorial noise propagation determined using 10 years of data from the Cluster spacecraft. *Journal of Geophysical Research: Space Physics*, *118*, 7160–7169. https://doi.org/10.1002/2013JA019373

Naitou, H., Kamimura, T., & Tokuda, S. (1979). On boundary conditions for a simulation plasma in a magnetic field. *Journal of Computational Physics*, *33*, 86–101. https://doi.org/10.1016/0021-9991(79)90029-9

Perraut, S., Roux, A., Robert, P., Gendrin, R., Sauvaud, J.-A., Bosqued, J.-M., et al. (1982). A systematic study of ULF waves above F/H plus/ from GEOS 1 and 2 measurements and their relationships with proton ring distributions. *Journal of Geophysical Research*, *87*, 6219–6236. https://doi.org/10.1029/JA087iA08p06219

Posch, J. L., Engebretson, M. J., Olson, C. N., Thaller, S. A., Breneman, A. W., Wygant, J. R., et al. (2015). Low-harmonic magnetosonic waves observed by the van allen probes. *Journal of Geophysical Research: Space Physics*, *120*, 6230–6257. https://doi.org/10.1002/2015JA021179

Roederer, J. G. (1970). *Dynamics of Geomagnetically Trapped Radiation*. Berlin: Physics and Chemistry in Space, Springer.

Russell, C. T., Holzer, R. E., & Smith, E. J. (1970). OGO 3 observations of ELF noise in the magnetosphere: 2. The nature of the equatorial noise. *Journal of Geophysical Research*, *75*, 755. https://doi.org/10.1029/JA075i004p00755

Santolík, O., Nemec, F., Gereová, K., Macúšová, E., Conchy, Y., & Cornilleau-Wehrlin, N. (2004). Systematic analysis of equatorial noise below the lower hybrid frequency. *Annales Geophysicae*, *22*, 2587–2595. https://doi.org/10.5194/angeo-22-2587-2004

Santolík, O., Parrot, M., & Němec, F. (2016). Propagation of equatorial noise to low altitudes: Decoupling from the magnetosonic mode. *Geophysical Research Letters*, *43*, 6694–6704. https://doi.org/10.1002/2016GL069582

Santolík, O., Pickett, J. S., Gurnett, D. A., Maksimovic, M., & Cornilleau-Wehrlin, N. (2002). Spatiotemporal variability and propagation of equatorial noise observed by Cluster. *Journal of Geophysical Research*, *107*, 1495. https://doi.org/10.1029/2001JA009159

Shklyar, D. R., & Balikhin, M. A. (2017). Whistler mode waves below lower hybrid resonance frequency: Generation and spectral features. *Journal of Geophysical Research: Space Physics*, *122*, 10,072–10,083. https://doi.org/10.1002/2017JA024416

Sun, J., Gao, X., Lu, Q., Chen, L., Liu, X., Wang, X., et al. (2017). Spectral properties and associated plasma energization by magnetosonic waves in the Earth's magnetosphere: Particle-in-cell simulations. *Journal of Geophysical Research: Space Physics*, *122*, 5377–5390. https://doi.org/10.1002/2017JA024027

Swift, D. W. (2007). Generalized curvilinear coordinates in hybrid and electromagnetic codes. In H. Usui, & Y. Omura (Eds.), *Advanced methods for space simulations* (pp. 77–89). Tokyo: TERRAPUB.

Tsurutani, B. T., Falkowski, B. J., Pickett, J. S., Verkhoglyadova, O. P., Santolik, O., & Lakhina, G. S. (2014). Extremely intense ELF magnetosonic waves: A survey of polar observations. *Journal of Geophysical Research: Space Physics*, *119*, 964–977. https://doi.org/10.1002/2013JA019284

Umeda, T., Omura, Y., & Matsumoto, H. (2001). *Computer Physics Communications*, *137*, 286–299. https://doi.org/10.1016/S0010-4655(01)00182-5

Xiao, F., & Feng, X. (2006). Modeling density and anisotropy of energetic electrons along magnetic field lines. *Plasma Science and Technology*, *8*, 279–284. https://doi.org/10.1088/1009-0630/8/3/07

Zhima, Z., Chen, L., Fu, H., Cao, J., Horne, R. B., & Reeves, G. (2015). Observations of discrete magnetosonic waves off the magnetic equator. *Geophysical Research Letters*, *42*, 9694–9701. https://doi.org/10.1002/2015GL066255